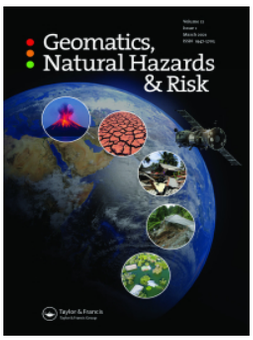

Geomatics, Natural Hazards and Risk

ISSN: (Print) (Online) Journal homepage: https://www.tandfonline.com/loi/tgnh20

Integration of ground-based and space-borne radar observations for three-dimensional deformations reconstruction: application to Luanchuan mining area, China

Zhenhai Wang, Jun Hu, Yaogang Chen, Xiling Liu, Jihong Liu, Wenqing Wu & Yanping Wang

To cite this article: Zhenhai Wang, Jun Hu, Yaogang Chen, Xiling Liu, Jihong Liu, Wenqing Wu & Yanping Wang (2022) Integration of ground-based and space-borne radar observations for three-dimensional deformations reconstruction: application to Luanchuan mining area, China, Geomatics, Natural Hazards and Risk, 13:1, 2819-2839, DOI: 10.1080/19475705.2022.2134828

To link to this article: https://doi.org/10.1080/19475705.2022.2134828

Published online: 22 Oct 2022.

GEOMATICS, NATURAL HAZARDS AND RISK
2022, VOL. 13, NO. 1, 2819–2839
https://doi.org/10.1080/19475705.2022.2134828

Taylor & Francis
Taylor & Francis Group

Integration of ground-based and space-borne radar observations for three-dimensional deformations reconstruction: application to Luanchuan mining area, China

Zhenhai Wang[a], Jun Hu[a,b], Yaogang Chen[a], Xiling Liu[c], Jihong Liu[a], Wenqing Wu[a] and Yanping Wang[d]

[a]School of Geosciences and Info-physics, Central South University, Changsha, China; [b]Key Laboratory of Metallogenic Prediction of Nonferrous Metals and Geological Environment Monitoring, Central South University, Ministry of Education, Changsha, China; [c]School of Resources and Safety Engineering, Central South University, Changsha, China; [d]Radar Monitoring Technology Laboratory, School of Information Science and Technology, North China University of Technology, Beijing, China

ABSTRACT

Luanchuan mining area, which is located in Henan Province, China and characterized by undulating topography and large precipitation, is vulnerable to the landslide disasters. The observations from the space-borne radar (ascending and descending TerraSAR-X) images and the ground-based radar (GPRI-II) images are integrated to monitor the surface deformations in Luanchuan mining area. Before the integration of the observations from multi-source SAR images, the coordinate systems of multi-source images are required to be unified by geographical projection. However, the accuracy of the commonly used geographical coding will be degraded by external DEM errors and inaccurate satellite orbit, which makes it difficult to achieve the high-precision registration of space-borne and ground-based radar scenes. Therefore, in this paper the iterative closest point (ICP) method is introduced to register the space-borne and ground-based images, yielding sub-pixel registration accuracy. Reasonable weights are then assigned to multi-source observations through Strain Model and Variance Component Estimation (SM-VCE) method, from which the high-precision three-dimensional deformations can be reconstructed. The results show that the maximum deformation rates in the east-west, north-south and vertical directions of Luanchuan mining area from July 20, 2019, to August 1, 2019, are about 0.2, 0.4 and 0.7 mm/day, respectively. The deformations are mainly on the loose slags in the Luanchuan pit rather than the bedrock, as a result of the accumulation of waste slags. Some suggestions on the installation location of ground-based radar are also provided to better combine the space-borne and ground-based observations.

ARTICLE HISTORY
Received 28 July 2022
Accepted 7 October 2022

KEYWORDS
ICP; SM-VCE; ground-based radar; space-borne SAR; 3D deformations

CONTACT Jun Hu csuhujun@csu.edu.cn

1. Introduction

Landslide disasters often cause huge losses to society due to their concealment and suddenness (Zhao et al. 2018; Lacroix et al. 2020), which not only affect normal production activities, but also seriously threaten human life (Hilley et al. 2004; Giordan et al. 2017). It is acknowledged that surface deformation is an important indicator of landslide disasters, which can be predicted by effectively identifying and monitoring deformation of the slow-moving landslide. In recent years, the development of Interferometric Synthetic Aperture Radar (InSAR) technology has provided new means for the monitoring of landslide (Riedel and Walther 2008; Zhang et al. 2018; Zhang et al. 2020). Space-borne InSAR can perform rapid, large-scale and low-cost monitoring with theoretical accuracy of millimeter level (Zhang et al. 2018; Solari et al. 2018; Ghadimi 2022), which is suitable for grasping long-term deformation trend of landslides (Kang et al. 2017; Rosi et al. 2018; Zhao et al. 2018). However, since the current SAR satellites flight in sun-synchronous orbit, space-borne InSAR is quite insensitive to north-south deformations (Pepe and Calò 2017; Zheng et al. 2021). The emergence and development of ground-based radars provide a chance to overcome the limit of space-borne InSAR (Noferini et al. 2007; Caduff et al. 2015; Wang et al. 2020). Since ground-based radars can flexibly choose the installation location, it is easier to capture north-south deformations with theoretical accuracy of sub-millimeter (Luo et al. 2014; Hu et al. 2019; Wang et al. 2020). In addition, the observation time interval of ground-based radar can be as short as a few minutes (Aguasca et al. 2004; Rödelsperger et al. 2010;), short-term emergency disaster monitoring can thus be carried out (Ferrigno et al. 2017).

In recent decades, many scholars had combined space-borne and ground-based interferometric radars to monitor surface deformation (Carlà et al. 2019; Wang et al. 2021). The initial idea is to monitor the deformations with different periods and frequencies by using space-borne and ground-based radars, which together serve the stability analysis of landslides. In 2004, the space-borne ERS-1/2 data from 1994 to 2001 and the ground-based Linear Synthetic Aperture high-resolution radar (LISA) data in 2002 have been employed to monitor landslide in the Rocca Pitigliana region. In 2006, 5-year long-term monitoring and 15-day emergency monitoring of Ponte Dolo' landslide have been carried out by space-borne ERS-1/2 scenes and ground-based LISA data, respectively (Corsini et al. 2006). In 2014, various data were used in the landslide mapping of the San Fratello test site, including ERS-1/2, ENVISAT, RADARSAT-1, COSMO-SkyMed as well as the ground-based LISA data (Bardi et al. 2014). In 2016, space-borne Sentinel-1 data spanning 9 months and short-term emergency ground-based radar data were used to monitor an undisclosed open-pit mine (Hilley et al. 2004). In 2018, COSMO-SkyMed and ground-based radar scenes were exploited to analyze the deformation of the Stromboli volcano in Italy and obtained a more complete deformation field (Carlà et al. 2018). In 2020, long-term space-borne sentinel-1 data and ground-based radar data were used for observations of the Mendatica landslide at Monesi (Navarro et al. 2020). In 2021, the Zhongbao landslide occurred in China, the ground-based radar was used for emergency monitoring, and then the Sentinel-1 data was used to obtain the deformation field after the landslide occurred (Xiao et al. 2021).

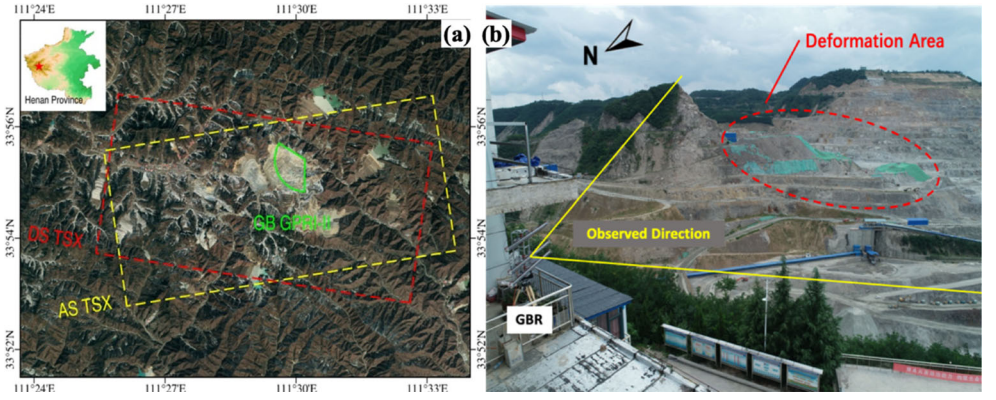

Figure 1. (a) Ground-based and space-borne radar image coverages. (b) Observed direction of ground-based radar.

The above research studies of integrating space-borne and ground-based interferometry to identify and characterize landslides are of great value. However, in such research studies, the two data were independently used for landslide interpretation, and complete three-dimensional (3D) deformations could not be obtained to reveal more detailed information. In order to overcome this challenge, recently some scholars had combined space-borne and ground-based radar data to calculate 3D deformations. In 2020, the ground-based Gamma Portable Radar Interferometer (GPRI) and space-borne COSMO-SkyMed radar observations had been integrated to monitor 3D deformations of the slope after the 2018 Baige landslide in China in order to assess its residual risk (Li et al. 2020). This work achieves the registration of space-borne and ground-based images by using the classical geographic projection. Limited by the accuracy of geocoding, the geographic projection is difficult to achieve sub-pixel registration accuracy, which is critical for high-precision 3D deformations. In 2021, a detailed analysis of the Stromboli Volcano in Italy had been conducted by using space-borne Sentinel-1 data to reveal the state before and after the volcanic eruption, and using ground-based radar data to reveal the relationship between volcanic eruption activity and deformation field (Di Traglia et al. 2021). In this work, the space-borne and ground-based radar observations are processed with equal weights when calculating the 3D deformations. However, in fact, the monitoring accuracies of the space-borne and ground-based data are different, and therefore the equal weight processing reduces the accuracies of the 3D deformations.

In this study, complete 3D deformation rates of the slow-moving landslides in Luanchuan mining area, China, are estimated by combining ground-based GPRI-II and space-borne TerraSAR-X radar observations. However, both space-borne and ground-based images have geocoding errors. The traditional method, i.e., geographic projection, will lead to the inconsistency between the monitoring positions acquired from the space-borne and ground-based radars, and thus reduce the accuracies of 3D deformations. In order to obtain sub-pixel-level registration accuracy, in this paper, the iterative closest point (ICP) method (Wu et al. 2021) is first introduced. The algorithm regards the ground-based and space-borne monitoring points as point clouds, and matches the corresponding points in the 3D space. Then, the Strain Model and

Table 1. Parameters of the used ground-based GPRI-II data in the Luanchuan mining area.

Band	Min. distance	Max. distance	ΔRr	Δraz (at 1000m distance)	Temporal range	No. of scenes
Ku	50 m	1600 m	0.75 m	6.8 m	22/07/2019–28/07/2019	754

Variance Component Estimation (SM-VCE) method (Liu et al. 2018; Hu et al. 2021) is employed to assign reasonable weights to the observations of the ground-based and space-borne radars in an iterative manner. Compared with the equal-weight adjustment process, this method reduces the weight of low-precision deformation, which is beneficial to obtain the more accurate 3D deformation rates.

2. Study area and used data

2.1. Study area

We carried out the experiments in the Luanchuan mining area, Henan Province, China, which covers an area of about 1.5km^2 (Figure 1). The Luanchuan mining area is located between Xiong'er Mountain and Funiu Mountain in the eastern part of the Qinling Mountains. The terrain is relatively steep, and the slopes here are mostly above 35°. The highest elevation of the terrain in the Luanchuan mining area exceeds 1600 m, and the relative height differences range from ∼200 m to ∼500 m. The annual rainfall is more than 600 mm, and the rainy season is from July to September. The large summer precipitation in the area increases the moisture content inside the unstable soil, and then the gravity of the landslide mass increases, causing displacement along the sliding surface under the condition of steep terrain. For human safety and normal production, accurate 3D surface deformation rates are of great significance.

2.2. Ground-based radar data

In recent years, ground-based radar has been often used for landslide monitoring activities (Wang et al. 2020). In this study, the GPRI-II (Werner et al. 2010) was used to collect data. The instrument can realize 360-degree sweep imaging through a real aperture radar and can reach 10 km for the maximum monitoring distance. We collected 754 images in Luanchuan mining area from July 22, 2019 to July 28, 2019. In order to avoid damage of the GPRI-II, we did not collect data at night, so the collection of data was discontinuous. Table 1 shows the details of the parameters of the used GPRI-II data.

After SBAS-InSAR (Berardino et al. 2002) processing, the one-dimensional along line-of-sight (LOS) direction of the GPRI-II can be obtained. The GPRI-II was placed on the balcony of the office building located in the northeast of the mine. The green sector in Figure 1(a) shows the monitoring range of GPRI-II. Figure 1(b) shows the distribution of the ground-based radar and the monitoring field. The yellow line indicates the monitoring direction of the ground-based radar, and the red oval frame indicates the location of the main deformation area.

Table 2. Parameters of the used space-borne TerraSAR-X data in the Luanchuan mining area.

Band	Orbits	ΔRr	ΔRaz	Temporal range	No. of scenes
X	Ascending	0.91 m	0.85 m	21/07/2019–19/03/2020	13
X	Descending	0.91 m	0.87 m	20/07/2019–18/03/2020	12

2.3. Space-borne radar data

In order to obtain the multi-angle surface deformation characteristics of the Luanchuan mining area, 13 ascending and 12 descending TerraSAR-X radar scenes were collected from July 21, 2019 to March 19, 2020, and from July 20, 2019, to March 18, 2020, respectively. The parameters of the used space-borne data are shown in Table 2.

Due to the long-term mining, the real terrain in the mining area is quite different from the previous DEM. Therefore, the DEM obtained by the unmanned air vehicle (UAV) is used to remove phase components associated with terrain in the interferograms. The UAV DEM is detailed in the following Section. Figure 2(a,b) shows the interferetric pairs of ascending and descending orbits, respectively. Through the processing of TCP-InSAR, the LOS deformations of the ascending orbit from 2019.07.21 to 2019.08.01 and the descending orbit from 2019.07.20 to 2019.07.31 are obtained, respectively. These two periods are the highest coincidence time periods with the ground-based radar monitoring period from 2019.07.22 to 2019.07.28. The combination of these three data minimizes the deformation rates error caused by time difference.

2.4. Unmanned air vehicle data

In order to better remove the phase components related to terrain, and realize the geographical coding of space-borne and ground-based radar images, a DEM with high precision and high resolution is necessary. To obtain the DEM of Luanchuan mining area, we had first taken aerial photographs by UAV in July 23, 2019 and then conducted 3D modeling by Pix4Dmapper software.

The UAV model is built by DJI Wizard 4RTK. By connecting the network RTK, 101 airways were set and 6198 optical images were obtained. The course overlap and side overlap were both 80%, and the original photos were obtained by three operations. The UAV flight altitude is about 400 m and the camera inclination is 60°. We input these original photos and camera parameters into Pix4Dmapper software. After generating point cloud and texture, the DEM with the resolution of 1 m is reconstructed for the study area (Figure 3).

3. Methodology

In order to obtain high-precision 3D deformation rates, the ICP algorithm is firstly used to register the space-borne and ground-based radar scenes, and the SM-VCE algorithm is then employed to determine the weights of the multi-source observations and to obtain the high-precision 3D deformation rates. The flowchart of obtaining 3D deformation rates by using ICP and SM-VCE methods is shown in Figure 4.

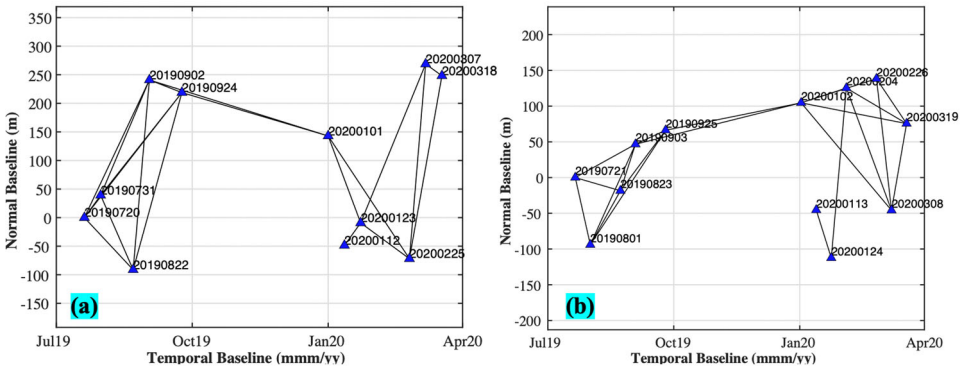

Figure 2. (a) Descending temporal and normal baselines. (b) Ascending temporal and normal baselines.

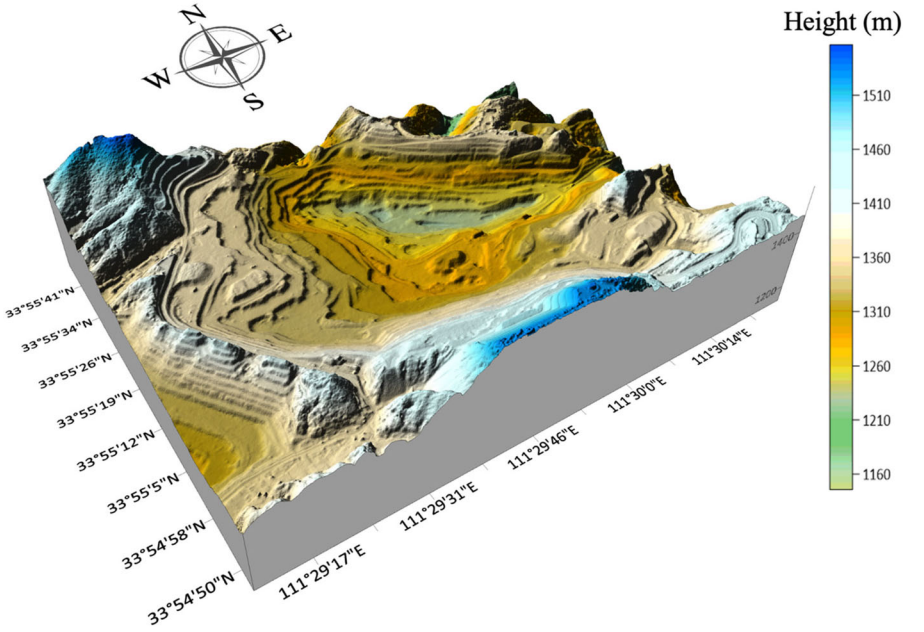

Figure 3. DEM produced by UAV.

3.1. Space-borne and ground-based image registration by ICP

Generally, the imaging geometries of space-borne and ground-based radar are quite different. It is therefore difficult to select corresponding points by using traditional two-dimensional matching algorithms such as gray-scale cross-correlation algorithm. The traditional geographical projection method is also difficult to work since the accuracy of geographical coding will be affected by the external DEM errors and satellite orbit errors.

Therefore, the ICP algorithm (Wu et al. 2021) was used for space-borne and ground-based image registration in this study. ICP is a classic algorithm for 3D laser point cloud registration. Two point clouds are continuously translated and rotated to achieve the best rigidity coincidence. Assuming that there is a main point cloud $Q = (q_1, q_2 \ldots q_m)$

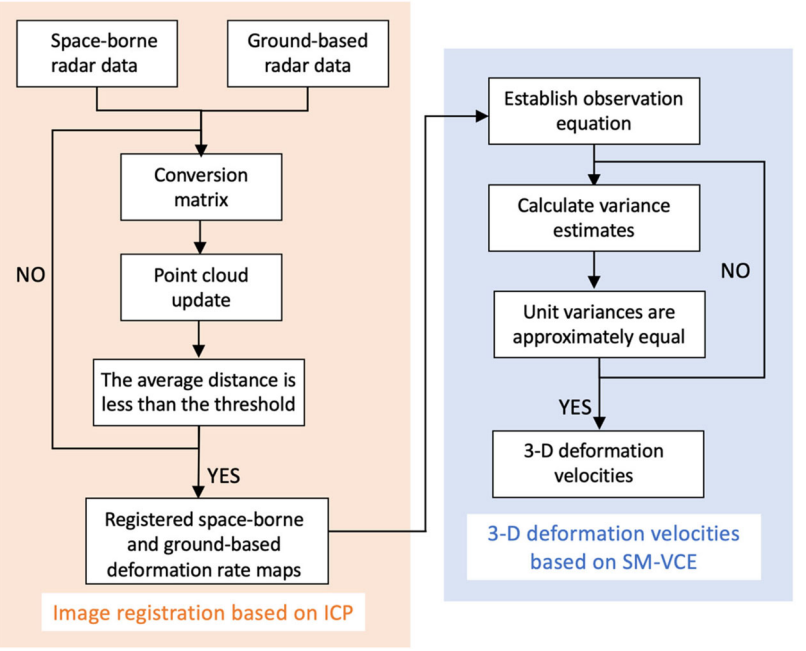

Figure 4. Flowchart of obtaining 3D deformation velocities by using ICP and SM-VCE methods.

composed of m points, and a secondary point cloud $P = (p_1, p_2 \ldots p_n)$ composed of n points, where $q_i = [x_{qi}\ y_{qi}\ z_{qi}](i = 1, 2 \ldots m), p_j = [x_{pj}\ y_{pj}\ z_{pj}](j = 1, 2 \ldots n)$, x、y、z indicate points in the east-west, north-south, and vertical directional position, respectively. Then, the spatial distance between p_j and Q is calculated. The point q_j in Q with the shortest spatial distance from p_j is regarded as the corresponding point of p_j.The relationship between p_j and q_j can be expressed by the following formula

$$q_j = R \cdot p_j + T \tag{1}$$

where R represents the rotation matrix, $T = [t_{xj}\ t_{yj}\ t_{zj}]^T$ represents the translation matrix, and t_x, t_y, t_z represents the amount of translation.

$$R = \begin{bmatrix} 1 & 0 & 0 \\ 0 & \cos\alpha & \sin\alpha \\ 0 & -\sin\alpha & \cos\alpha \end{bmatrix} \cdot \begin{bmatrix} \cos\beta & 0 & -\sin\beta \\ 0 & 1 & 0 \\ \sin\beta & 0 & \cos\beta \end{bmatrix} \cdot \begin{bmatrix} \cos\gamma & \sin\gamma & 0 \\ -\sin\gamma & \cos\gamma & 0 \\ 0 & 0 & 1 \end{bmatrix} \tag{2}$$

Here, α, β and γ represent the rotation angles in the east-west, north-south, and vertical directions, respectively. R and T can be solved when the following formula is satisfied

$$\min \frac{1}{n} \sum_{j=1}^{n} ||q_j - (R \cdot p_j + T)||^2 \tag{3}$$

After solving R and T, let $p_j^{'} = R \cdot p_j + T$ denote the updated p_j. The following formula is used to calculate the average distance between the master point cloud and the updated slave point cloud.

$$d = \frac{1}{n}\sum_{j=1}^{n} ||p_j^{'} - q_j||^2 \tag{4}$$

If d is less than a certain distance, the calculation is terminated, otherwise, $p_j^{'}$ is substituted into the above equation to calculate R and T again until d is less than a certain distance or the iterations reach the preset number. After the calculation is terminated, n nearest neighbor point pairs are formed. The corresponding points are selected according to the spatial distances between the nearest point pairs. According to the differences of the horizontal and vertical coordinates of corresponding points, the image registration polynomial is calculated by the least square method to complete the image registration process.

3.2. Three-dimensional deformations estimation by SM-VCE

SM-VCE is a method to retrieve 3D deformation rates from the integration of heterogeneous InSAR observations (Liu et al. 2018). It has been successfully applied to the weight determination of multi-platform space-borne observations (Hu et al. 2012; Hu et al. 2021). Since the ground-based and space-borne radar observations have different degrees of noise level, it is inappropriate to perform equal weighting of the two kinds of data in the estimating of 3D deformation rates. The variance component estimation (VCE) algorithm is used here to determine the weights of the ground-based and space-borne observations. In order to meet the requirement of VCE for the redundant observations, the stress-strain model (SM) is used to increase space-borne and ground-based observations by establishing the relationship between the deformation of a certain point and the deformations of the nearby points

By projecting the radar observations of surrounding points to the center point, the redundant observations are obtained, which are useful in the determination of the weight. Assuming that there is a point a_0 in the deformation area, a window is opened with a_0 as the center (e.g., 50 m × 50 m), and there are K points $a_i(\mathrm{i} = 1...\mathrm{K})$ inside the window. Suppose the 3D deformations of a_0 and a_i are $d_0 = [d_{0(e)}\ d_{0(n)}\ d_{0(u)}]$ and $d_i = [d_{i(e)}\ d_{i(n)}\ d_{i(u)}]$, respectively, and the 3D spatial positions are $[x_{0(e)}\ x_{0(n)}\ x_{0(u)}]$ and $[x_{i(e)}\ x_{i(n)}\ x_{i(u)}]$, respectively. According to the stress-strain model,

$$d_i = (E + \Omega) \cdot \Delta_i + d_0 \tag{5}$$

where $E = \begin{bmatrix} \varepsilon_{11} & \varepsilon_{12} & \varepsilon_{13} \\ \varepsilon_{12} & \varepsilon_{22} & \varepsilon_{23} \\ \varepsilon_{13} & \varepsilon_{23} & \varepsilon_{33} \end{bmatrix}$ means strain tensor, $\Omega = \begin{bmatrix} 0 & -\omega_3 & \omega_2 \\ \omega_3 & 0 & -\omega_1 \\ -\omega_2 & \omega_1 & 0 \end{bmatrix}$ means rigid body rotation tensor. Eq. (5) can be rewritten as

$$d_i = B_{sm(i)} \cdot l \tag{6}$$

where $l = [d_{0e}\ d_{0n}\ d_{0u}\ \varepsilon_{11}\ \varepsilon_{12}\ \varepsilon_{13}\ \varepsilon_{22}\ \varepsilon_{23}\ \varepsilon_{33}\ \omega_1\ \omega_2\ \omega_3]^{\mathrm{T}}$, contains all the unknown parameters that need to be solved, $B_{sm(i)}$ is a design matrix. At point a_0, the observed value of ascending space-borne, descending space-borne and ground-based radars is

$L_i = [L_{as(i)}\ L_{ds(i)}\ L_{gb(i)}]^T$. The relationship between the observed measurement L_i and the 3D deformation rates variable d_i can then be expressed by the following formula:

$$L_i = B_{geo(i)} \cdot d_i = B_{geo(i)} \cdot B_{sm(i)} \cdot l = B_{(i)} \cdot l \tag{7}$$

Combining all K points around a_0, it can be known that :

$$\underset{3K\times 1}{\mathrm{L}} + \underset{3K\times 1}{\mathrm{V}} = \underset{3K\times 12}{\mathrm{B}} \cdot \underset{12\times 1}{l} \tag{8}$$

Here V represents the residual vector, L represents the observation value vector, B represents the coefficient matrix and can be expressed by the following formula:

$$L = [(L_1)^T, (L_2)^T \cdots (L_K)^T] \tag{9}$$

$$B = [(B_1)^T, (B_2)^T \cdots (B_K)^T] \tag{10}$$

Equation (8) can be solved by the least squares (LS) algorithm. We use the VCE method to determine the weights of the three kinds of radar observations. The weights of the three groups of ascending space-borne, descending space-borne, and ground-based observations are W_{as}, W_{ds}, W_{gb}, respectively. The observations are L_{as}, L_{ds}, L_{gb}, and the coefficient matrix is B_{as}, B_{ds}, B_{gb}, respectively, where L_{as} and B_{as} are represented by L and B. The matrix consists of 1, 4, 7...3K − 2 rows. The initial weight matrix is set as the unit matrix. By solving Eq. (8), it can be known that

$$\begin{cases} l = N^{-1}H \\ v_{as} = B_{as} \cdot l - L_{as} \\ v_{ds} = B_{ds} \cdot l - L_{ds} \\ v_{gb} = B_{gb} \cdot l - L_{gb} \end{cases} \tag{11}$$

where $N = N_{as} + N_{ds} + N_{gb} = {B_{as}}^T W_{as} B_{as} + {B_{ds}}^T W_{ds} B_{ds} + {B_{gb}}^T W_{gb} B_{gb}$, $H = {B_{as}}^T W_{as} L_{as} + {B_{ds}}^T W_{ds} L_{ds} + {B_{gb}}^T W_{gb} L_{gb}$. The relationship between the variance component and the observation residual is as follows:

$$\hat{\theta} = Q^{-1}\zeta_\theta \tag{12}$$

where $\hat{\theta} = [\hat{\sigma}_{as}^2\ \hat{\sigma}_{ds}^2\ \hat{\sigma}_{gb}^2]^T$, $\zeta_\theta = [v_{as}^T W_{as} v_{as}\ v_{ds}^T W_{ds} v_{ds}\ v_{gb}^T W_{gb} v_{gb}]^T$. The variance component $\hat{\theta}$ will be used to obtain the updated weight matrix:

$$\hat{W}_{as} = W_{as},\ \ \hat{W}_{ds} = \frac{\hat{\sigma}_{as}^2}{\hat{\sigma}_{as}^2 W_{ds}^{-1}},\ \ \hat{W}_{gb} = \frac{\hat{\sigma}_{gb}^2}{\hat{\sigma}_{gb}^2 W_{gb}^{-1}} \tag{13}$$

The updated weight matrix is used to perform the LS operation again, and this process is repeated until the following condition is met:

$$\hat{\sigma}_{as}^2 \approx \hat{\sigma}_{ds}^2 \approx \hat{\sigma}_{gb}^2 \tag{14}$$

After obtaining the appropriate weights of ground-based and space-borne observations, the high-precision 3D deformation rates of point a_0 can be obtained.

3.3. Calculation of the DDOP value

The accuracies of 3D deformation rates are not only affected by the accuracies of the space-borne and ground-based radar observations, but also by the spatial distribution of the ascending, descending and ground-based radars. Therefore, the installation position of the ground-based radar is of great importance since the positions of the satellites are difficult to deploy. The concept of Deformation Dilution of Precision (DDOP) is used to determine which kind of distribution of multi-source radars is reasonable, and can be calculated as follows (Hu et al. 2021):

$$A = \begin{bmatrix} e_{as} & n_{as} & u_{as} \\ e_{ds} & n_{ds} & u_{ds} \\ e_{gp} & n_{gp} & u_{gp} \end{bmatrix} \tag{15}$$

$$Q = (A^T A)^{-1} = \begin{bmatrix} q_{11} & q_{12} & q_{13} \\ q_{21} & q_{22} & q_{23} \\ q_{31} & q_{32} & q_{33} \end{bmatrix} \tag{16}$$

$$\mathrm{DDOP} = \sqrt{q_{11} + q_{22} + q_{33}} \tag{17}$$

where e, n, and u represent the coefficients of the position coordinate components in the east-west, north-south, and vertical directions, respectively, and the subscripts as, ds, and gp represent the ascending orbiting satellite, the descending orbiting satellite, and the ground-based radar, respectively. The number of rows in A should be at least 3. The smaller the value of DDOP, the smaller the position errors in the east-west, north-south and vertical directions.

4. Results

4.1. Image registration between ground-based and space-borne data

In this study, the ascending radar image is used as the master image of the three kinds of data. In order to obtain the ascending point cloud, we need the original DEM and the ascending orbit topographic residuals. The aforementioned DEM obtained by UAV is used as the original DEM. Through 13 TerraSAR-X radar images, we obtain the topographic residuals of the ascending data. By combining the topographic residuals and the original DEM, the 3D positions of ascending point cloud are obtained.

In order to obtain the ground-based point cloud, we need the original DEM and the relative elevation converted from the terrain phase of the ground-based radar. For

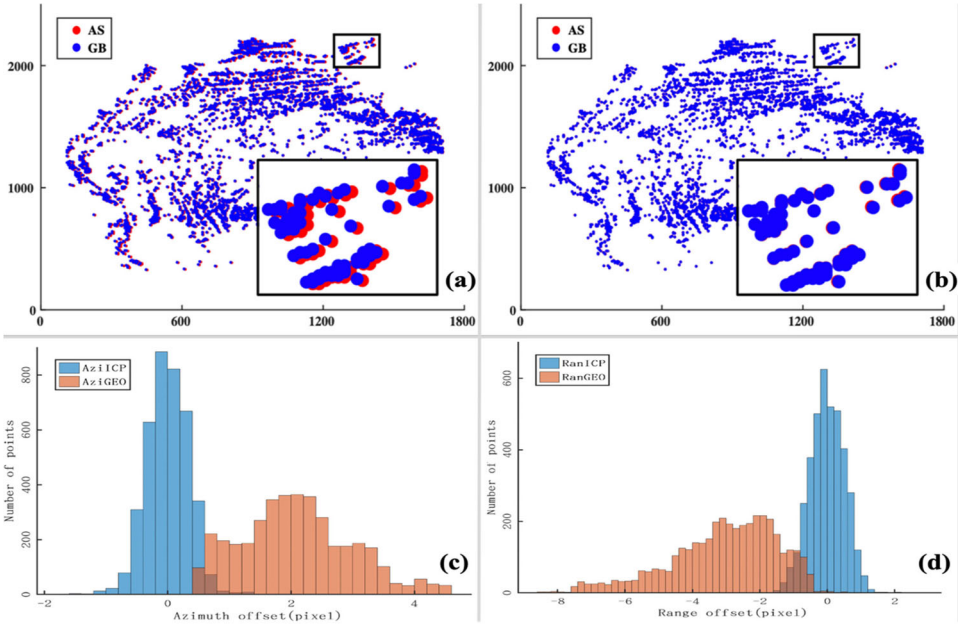

Figure 5. (a) and (b) show the corresponding points obtained by the traditional geographic projection method and the ICP method, respectively. (c) and (d) represent the statistics of the offsets of the two methods in the azimuth and the range directions, respectively.

ground-based radar fixed on the ground with a single receiving antenna, the terrain phase cannot be captured on the interferogram. Thanks to the fact that the GPRI-II has two receiving antennas, 3D terrain can be reconstructed by interfermetry of SAR images acquired by two receiving antennas. Similarly, by combining it with the original DEM, the 3D positions of ground-based point cloud are obtained.

The ICP method is used to continuously change the rigidity (translation, rotation) of the ground-based point cloud in the 3D space to achieve the best fit with the ascending point cloud. For each point in the ground-based point cloud, the corresponding point can be found in the ascending point cloud and the spatial distance between the two points can be calculated. The distance threshold will be used to filter out the points that are far enough. After selecting a set of corresponding points, the space-borne and ground-based images are registered by a polynomial, where the coefficients of the polynomial are obtained from these corresponding points by using LS adjustment.

Figure 5(a,b) shows the overlap maps of the point clouds obtained by the traditional geographic projection method and the ICP method, respectively. The red and blue points represent the corresponding points in the ascending and ground-based point clouds, respectively. Figure 5(c,d) shows the azimuth and range offsets of the corresponding points calculated by the two methods, respectively. In order to facilitate the display, the diameter of each point in Figure 5(c,d) is 10 pixels, in fact, each one only occupies 1 pixel. The horizontal and vertical coordinates in Figure 5(c,d) represent the row and column numbers of the geocoded ascending image. The orange and blue bars in Figure 5(c,d) show the offsets of the traditional geographic

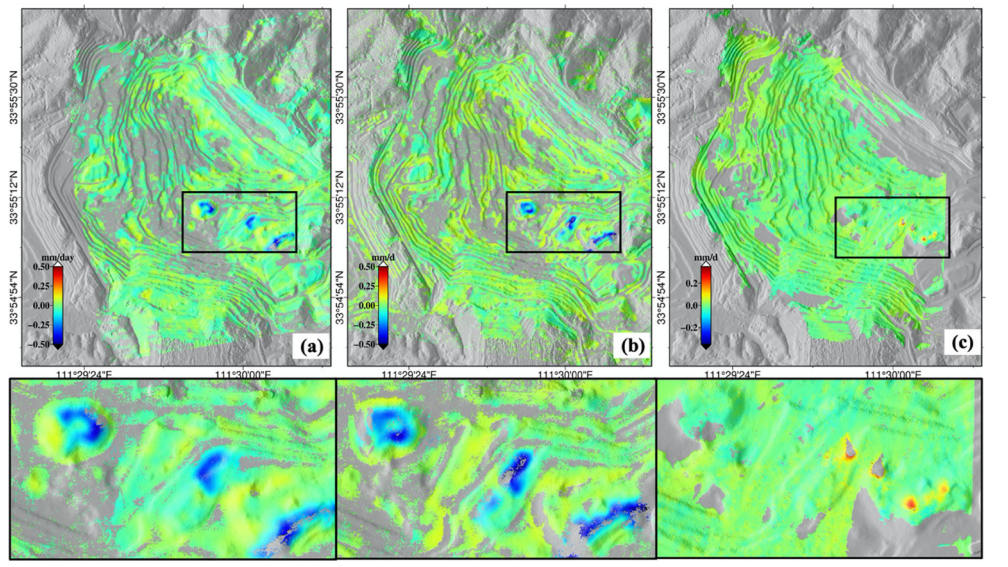

Figure 6. (a) Ascending deformation rate during 20190721-20190801. (b) Descending deformation rate during 20190720-20190731. (c) Ground-based deformation rate during 20190722-20190728.

projection method and the ICP method, respectively. It is found that the traditional projection method gets a maximum offset of 7 pixels. This means that space-borne and ground-based images are not registered, leading to additional errors in the calculation of the 3D deformation rates. After registration by the ICP method (Figure 5(d)), the registration deviation of most points with the corresponding points is within one pixel. Subpixel registration accuracy is crucial for the subsequent estimation of 3D deformation rates.

4.2. Los deformation rates of space-borne and ground-based radars

We obtained 13 ascending TerraSAR-X images from July 21, 2019 to March 19, 2020 and 12 descending TerraSAR-X images from July 20, 2019 to March 18, 2020, respectively. The TCP-InSAR algorithm has been applied to the processing of space-borne SAR data. After the image registration, the selection of interferometric pairs, the removal of terrain phase and the parameter calculation, the LOS deformation rates of the ascending orbit (Figure 6(a)) and the descending orbit (Figure 6(b)) are obtained, respectively. Interferometric pairs of ascending and descending orbits can be found in Figure 2. Three main deformation regions can be identified in space-borne radar observations. It is found that the deformations are far away from the satellite. The maximum deformation rates of the ascending and descending orbits are about 0.5 mm/day and 0.6 mm/day, respectively.

754 images are collected by the GPRI-II from July 22, 2019 to July 28, 2019, which are processed by the SBAS-InSAR algorithm. The average LOS deformation rate during this period is solved by constructing interferometric pairs, filtering interferogram, phase unwrapping and parameter calculation. The monitoring results of the ground-based radar are shown in Figure 6(c). Two main deformation regions are detected by

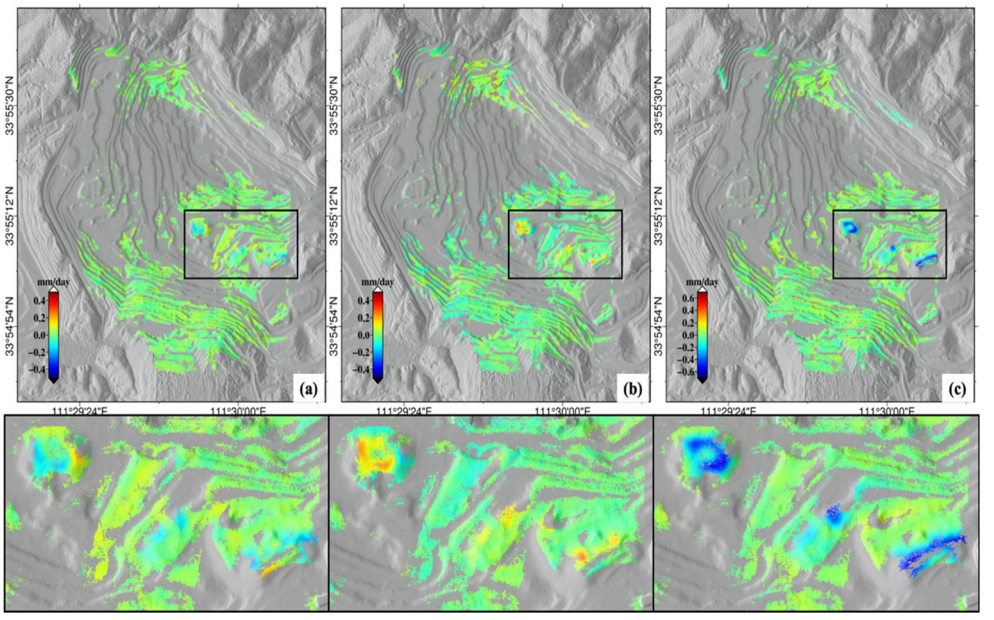

Figure 7. (a) E-W deformation rate, (b) N-S deformation rate, (c) U-D deformation rate.

ground-based radar. The deformations in Figure 6(c) are all positive, indicating that the surface moves toward the ground-based radar, and the maximum deformation rate is about 0.4 mm/day.

We can observe more detailed deformation characteristics in the enlarged graph below Figure 6. The northwest corner in the black box shows obvious deformation signals in the space-borne observations, but no deformation signals in the ground-based observation. Considering that the ground-based radar is placed northeast of the deformation area, the current imaging geometry of ground-based radar is not sensitive to the direction of deformation. Except the deformation regions in the black box in Figure 6, other regions in the mining area are basically stable. However, since the terrain of the mining area is quite undulating (Figure 3), there are some shadows in the space-borne and ground-based radar images, yielding incomplete deformation rate results.

4.3. Three-dimensional deformation rates

Figure 7(a–c) shows the east-west, north-south and up-down deformation rates of the Luanchuan mining area, respectively. It can be found in Figure 7 that there are no more deformation regions except those in the black box, which is consistent with the stable regions in Figure 6. In addition, the number of monitoring points in Figure 7 is less than that in Figure 6. This is expected since we extract the intersection points of the ascending, descending and ground-based radar observations to calculate the 3D deformation rates.

Figure 8 shows the 3D deformation rates of the area outlined by the black box in Figure 7. To facilitate the description of the three deformation regions, the three

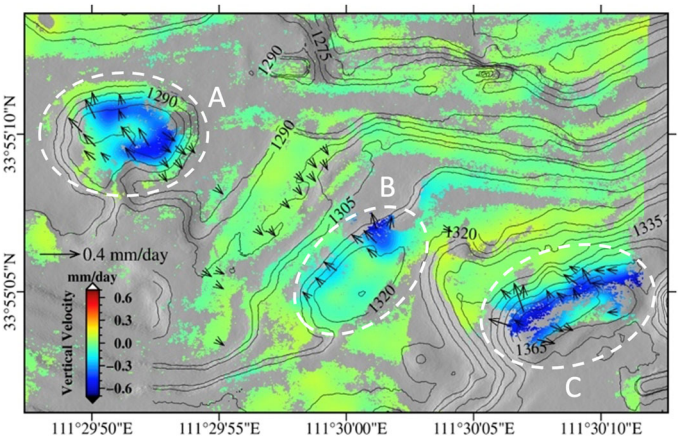

Figure 8. 3D deformation rates of the deformation region.

main deformation regions are termed A, B, and C, respectively, as shown in the white circle in Figure 8. In order to exhibit the deformation of the regions more clearly, the 3D deformation rates of the regions A, B and C are shown in stereo perspective in Figure 9(a–c), respectively. The east-west and north-south length of region A are about 165 m and 110 m, respectively, and the elevation difference is about 20 m. The terrain of region A is convex in the middle and flat around (Figure 9(a)). The deformation rates distributed in A region behave as an unclosed ring. From Figure 9(a), we find that the deformation region is mainly concentrated at the top of the slope. The direction of displacement is from the middle area of A to the surrounding. The maximum east-west, north-south, and up-down deformation rates are 0.2 mm/day, 0.4 mm/day, and 0.5 mm/day, respectively. The lengths of the east-west and north-south of region B are about 140 m and 150 m, respectively, and the elevation difference is about 14 meters. The south-east terrain is high and the north-west terrain is low (Figure 9(b)). The deformation is concentrated in the northeast corner of the region B. The maximum east-west, north-south, and up-down deformation rates are about 0.1 mm/day, 0.2 mm/day, and 0.6 mm/day, respectively. The lengths of east-west and north-south in region C are about 210 m and 140 m, respectively, and the elevation difference is about 32 m. The middle terrain is high and the surrounding terrain is low (Figure 9(c)). The deformation area is distributed like a strip, which is located at the top of the slope. The maximum east-west, north-south, and up-down deformation rates are about 0.2 mm/day, 0.4 mm/day, and 0.7 mm/day, respectively.

5. Results

5.1. Analysis of the threat of deformation

In order to evaluate the deformation hazard of regions A, B and C, we show the main sliding directions of the deformations in Figure 10, as provided by the 3D deformation rates estimated from the integration of ground-based and space-borne radar observations. The elevation and optical image of the 3D model are obtained by UAV. Although the surface displacements are found at the top of the slope in regions

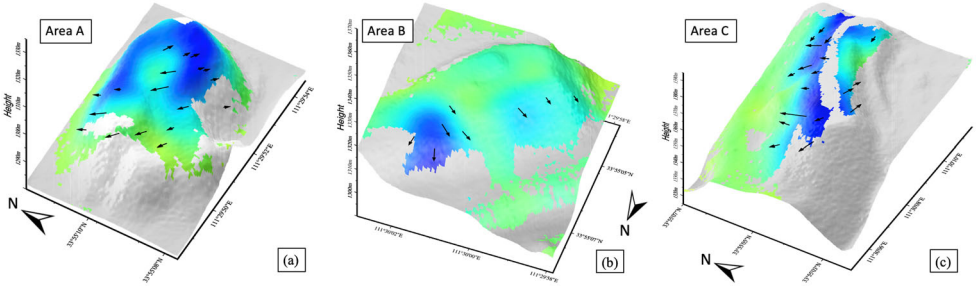

Figure 9. (a–c) 3D deformation rates of regions A, B, and C.

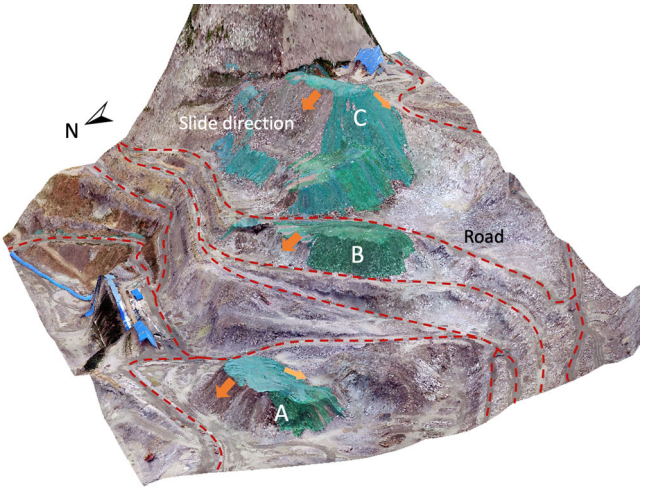

Figure 10. Slide directions of the deformations in regions A, B, and C.

A, B and C, there are no obvious surface ruptures due to the small cumulative deformation. The red dotted lines in Figure 10 indicate the main roads in the mining area. The green area in Figure 10 is the area covered by dustproof nets. Although the deformation areas are relatively close to the roads in the mining area, it is difficult for the landslide body to have a large impact on the traffic in the mining area due to its small volume. In Figure 10, we can see that the nearby artificial buildings (e.g., blue houses) are far away from the landslide, so the threat of the landslide is low. It can be known from the prior information that regions A, B and C are mainly located at the bottom of the pit, and its causes are related to the accumulation of waste slags. Therefore, the deformations are on the loose slags in the pit rather than the bedrock.

5.2. Analysis of the installation position of the ground-based radar

Small value of DDOP means good distribution of the radars to obtain high-precision 3D deformation rates. Generally speaking, the larger the volume of the unit triangular pyramid composed of the ascending, descending, ground-based radars and ground points, the lower the spatial correlation of the three observations, and the smaller value of the DDOP. The DDOP values of Luanchuan mining area are shown in

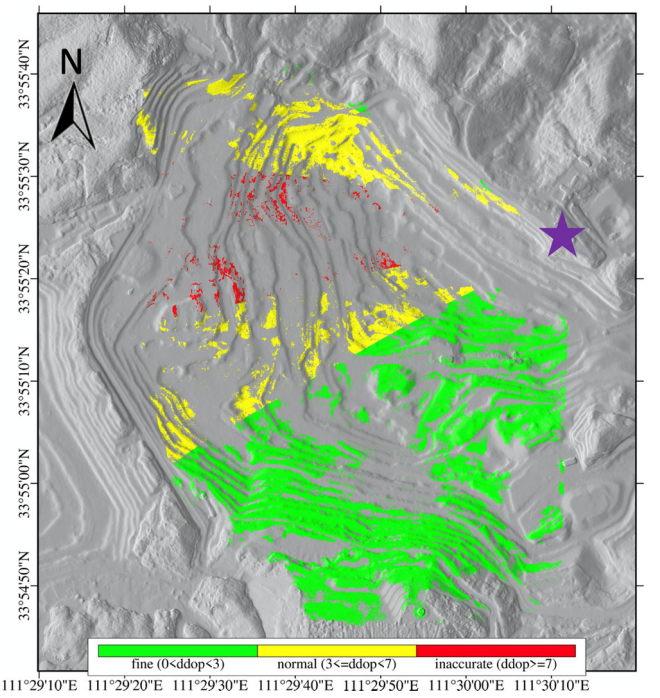

Figure 11. DDOP values of Luanchuan mining area. Purple star shows the location of the ground-based radar.

Figure 11. It can be observed that the distribution of the three radars in the areas with the DDOP value less than 3 is the most reasonable. The radar distribution in the areas with the DDOP value greater than 7 is unreasonable, where the observations should be discarded.

The purple triangle in Figure 11 represents the location of the ground-based radar. It can be found that when the red area is monitored, the sight direction of ground-based radar is approximately parallel to the east-west direction. The monitoring directions of space-borne radars are fixed, which are also approximately parallel to the east-west direction. Under this monitoring geometry, it is difficult for both ground-based and spaceborne radars to capture the north-south deformation. Therefore, the radar observation geometry of the radars in Figure 11 is not ideal for the slopes in the red region. Therefore, when we lay the ground-based radar, in addition to consider the field environment, the radar should be installed in the north-south direction of the interested deformation region as possible, so as to provide ideal supplementary observations for space-borne radars.

5.3. Suggestions of the installation position of two ground-based radars

Through the analysis of Section 5.2, we can know that when only a single ground-based radar is used, sufficient accuracies of the 3D deformation rates cannot be guaranteed for all monitoring points. Therefore, we analyze how to deploy two ground-based radars

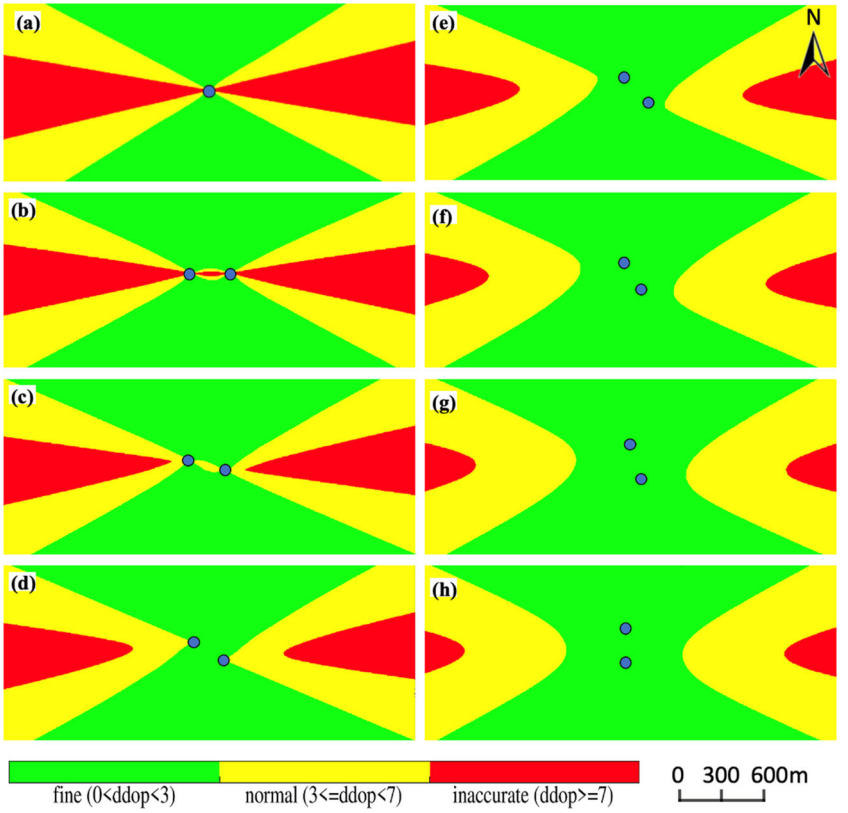

Figure 12. (a) DDOP values of one ground-based radar (b–h) DDOP values when the angles between the line direction of two ground-based radars and the west direction are 0°, 15°, 30°, 45°, 60°, 75°, 90°, respectively.

to increase the number of the monitoring points with DDOP <3 as much as possible and put forward some reasonable suggestions.

Figure 12(a) represents the DDOP values of one ground-based radar, the blue point represents the position of the ground-based radar. The green areas are the places characterized by high accuracy and the monitoring data in the red area are not available. Figure 12(b–h) represents the DDOP values under the deployment of two ground-based radars, and the angles between the line direction of two ground-based radars and the west direction are 0°, 15°, 30°, 45°, 60°, 75°, 90°, respectively. It can be seen that the accuracies of the points around the ground-based radars gradually increase as the angle changes from 0° to 90°. The DDOP values with the angles between the line direction and the east direction from 90° to 360° are not presented but can be easily deduced from Figure 12.

Therefore, the two ground-based radars should be laid in the north-south direction of the study area as far as possible. In this way, most points can achieve high accuracy when integrating the ground-based and space-borne radars observations for 3D deformations reconstruction. The distance between the two ground-based radars in Figure 12(b–h) is 300 m. With the changes in the distance, the green, yellow and red areas in Figure 12 will be scaled equally. Therefore, when the study area is large (e.g.,

more than 1 km), the distance between the two ground-based radars can be increased to obtain more monitoring points with high accuracy.

6. Summary

As an important indicator of landslide disasters, accurate 3D surface deformations are of great significance for early geological hazard identification. In the existing research of obtaining 3D deformations by combining space-borne and ground-based radars, the traditional geographic projection method is used to register the space-borne and ground-based radar images, and then the same weights are assigned to each observation to obtain the 3D deformations. The method of geographical projection is easily affected by DEM errors and satellite orbit errors, and it is difficult to achieve high-precision image registration between space-borne and ground-based data. In addition, since the space-borne and ground-based observations have different measurement accuracies, assigning them the same weight will reduce the accuracies of 3D deformations. Therefore, in this study, the ICP algorithm is first introduced to realize the fine registration of space-borne and ground-based images, and the SM-VCE algorithm is then used to define the precise weights of space-borne and ground-based observations and calculate high-precision 3D deformations.

This method has been successfully applied to the Luanchuan mining area, Henan Province, China. The experimental results show that the registration accuracy of space-borne and ground-based images can be better than 1 pixel by using the ICP algorithm. Compared with the registration accuracy of several pixels of traditional geographical projection, the registration accuracy of sub-pixel can better serve the estimations of 3D deformation results. Through the SM-VCE algorithm, more reasonable weights are assigned to the ground-based and space-borne radar observations, which yield high-precision 3D deformations of the Luanchuan mining area. The maximum deformation rates of east-west, north-south and up-down directions are 0.2 mm/day, 0.4 mm/day and 0.7 mm/day, respectively. Through the 3D deformations of the Luanchuan mining area, we analyze the risks of landslides in the mining area. Finally, the suggestions on the installation location of ground-based radar are given to better combine the space-borne and ground-based radar observations. Due to the limited time of the ground-based radar monitoring, this experiment did not achieve the acquisition of 3D deformation of time series. The observation time of the ground-based radar would be increased in the future to obtain 3D deformation of time series.

It has been proved that the combination of the space-borne and ground-based radars can provide the 3D surface deformations of landslide in the mining area. Since complete 3D deformations are of great significance for the investigating and interpreting of almost all kinds of geo-hazards, the combination of the space-borne and ground-based radars can play a vital role in many scenarios such as structural health monitoring, slope stability analysis, and glacier disaster prevention.

Disclosure statement

No potential conflict of interest was reported by the authors.

Funding

This study was supported by the National Natural Science Foundation of China (No. 42030112), the Nature Science Foundation of Hunan Province (No. 2020JJ2043), the Project of Innovation-driven Plan of Central South University (No. 2019CX007), the Fundamental Research Funds for the Central Universities of Central South University (No. 2020zzts176). The TerraSAR-X data were provided by the German Aerospace Center (DLR) under the general AO project (No. MTH3631).

Data availability statement

The data used to support the findings of this study are available from the corresponding author upon request.

References

Aguasca A, Broquetas A, Mallorquí JJ, Fabregas X. 2004. A solid state L to X-band flexible ground-based SAR system for continuous monitoring applications. IGARSS. 2:757–760.

Bardi F, Frodella W, Ciampalini A, Bianchini S, Del Ventisette C, Gigli G, Fanti R, Moretti S, Basile G, Casagli N. 2014. Integration between ground based and satellite SAR data in landslide mapping: The San Fratello case study. Geomorphology. 223:45–60.

Berardino P, Fornaro G, Lanari R, Sansosti E. 2002. A new algorithm for surface deformation monitoring based on small baseline differential SAR interferograms. IEEE Trans Geosci Remote Sensing. 40(11):2375–2383.

Caduff R, Schlunegger F, Kos A, Wiesmann A. 2015. A review of terrestrial radar interferometry for measuring surface change in the geosciences. Earth Surf Process Landforms. 40(2): 208–228.

Carlà T, Farina P, Intrieri E, Ketizmen H, Casagli N. 2018. Integration of ground-based radar and satellite InSAR data for the analysis of an unexpected slope failure in an open-pit mine. Eng Geol. 235:39–52.

Carlà T, Tofani V, Lombardi L, Raspini F, Bianchini S, Bertolo D, Thuegaz P, Casagli N. 2019. Combination of GNSS, satellite InSAR, and GBInSAR remote sensing monitoring to improve the understanding of a large landslide in high alpine environment. Geomorphology. 335:62–75.

Corsini A, Farina P, Antonello G, Barbieri M, Casagli N, Coren F, Guerri L, Ronchetti F, Sterzai P, Tarchi D. 2006. Space-borne and ground-based SAR interferometry as tools for landslide hazard management in civil protection. Int J Remote Sens. 27(12):2351–2369.

Di Traglia F, De Luca C, Manzo M, Nolesini T, Casagli N, Lanari R, Casu F. 2021. Joint exploitation of space-borne and ground-based multitemporal InSAR measurements for volcano monitoring: The Stromboli volcano case study. Remote Sens Environ. 260:112441.

Ferrigno F, Gigli G, Fanti R, Intrieri E, Casagli N. 2017. GB-InSAR monitoring and observational method for landslide emergency management: the Montaguto earthflow (AV, Italy). Nat Hazards Earth Syst Sci. 17(6):845–860.

Ghadimi M. 2022. Investigation of riprap stability of a dam: risk assessment by InSAR method and rock mechanical test. Geomatics Nat Hazards Risk. 13(1):1441–1456.

Giordan D, Manconi A, Remondino F, Nex F. 2017. Use of unmanned aerial vehicles in monitoring application and management of natural hazards. Geomatics Nat Hazards Risk. 8(1):1–4.

Hilley GE, Burgmann R, Ferretti A, Novali F, Rocca F. 2004. Dynamics of slow-moving landslides from permanent scatterer analysis. Science. 304(5679):1952–1955.

Hu C, Deng Y, Tian W, Wang J, Zeng T. 2019. Novel MIMO-SAR system applied for high-speed and high-accuracy deformation measurement. J Eng. 2019(20):6598–6602.

Hu J, Li ZW, Sun Q, Zhu JJ, Ding XL. 2012. Three-dimensional surface displacements from InSAR and GPS measurements with variance component estimation. IEEE Geosci Remote Sens Lett. 9(4):754–758.

Hu J, Liu J, Li Z, Zhu J, Wu L, Sun Q, Wu W. 2021. Estimating three-dimensional coseismic deformations with the SM-VCE method based on heterogeneous SAR observations: Selection of homogeneous points and analysis of observation combinations. Remote Sens Environ. 255:112298.

Kang Y, Zhao C, Zhang Q, Lu Z, Li B. 2017. Application of InSAR techniques to an analysis of the Guanling landslide. Remote Sensing. 9(10):1046.

Lacroix P, Handwerger AL, Bièvre G. 2020. Life and death of slow-moving landslides. Nat Rev Earth Environ. 1(8):404–419.

Li Y, Jiao Q, Hu X, Li Z, Li B, Zhang J, Jiang W, Luo Y, Li Q, Ba R. 2020. Detecting the slope movement after the 2018 Baige Landslides based on ground-based and space-borne radar observations. Int J Appl Earth Obs Geoinf. 84:101949.

Liu JH, Hu J, Li ZW, Zhu JJ, Sun Q, Gan J. 2018. A method for measuring 3-D surface deformations with InSAR based on strain model and variance component estimation. IEEE Trans Geosci Remote Sensing. 56(1):239–250.

Luo Y, Song H, Wang R, Deng Y, Zhao F, Xu Z. 2014. Arc FMCW SAR and applications in ground monitoring. IEEE Trans Geosci Remote Sensing. 52(9):5989–5998.

Massimo B, Alessandro C, Nicola C, Paolo F, Franco C, Paolo S, Davide L, Dario T. 2004. Space-borne and ground-based SAR interferometry for landslide activity analysis and monitoring in the Appennines of Emilia Romagna (Italy): review of methods and preliminary results. ESA SP. 550:463–470.

Navarro JA, Luzi G, Monserrat O, Crosetto M. 2020. Ground-based & spaceborne SAR interferometric techniques supporting the management of emergencies in the Heimdall project. Int Arch Photogramm Remote Sens Spatial Inf Sci. XLIII-B3-2020:1685–1690.

Noferini L, Pieraccini M, Mecatti D, Macaluso G, Atzeni C, Mantovani M, Marcato G, Pasuto A, Silvano S, Tagliavini F. 2007. Using GB-SAR technique to monitor slow moving landslide. Eng Geol. 95(3-4):88–98.

Pepe A, Calò F. 2017. A review of interferometric synthetic aperture RADAR (InSAR) multi-track approaches for the retrieval of Earth's surface displacements. Applied Sciences. 7(12): 1264.

Riedel B, Walther A. 2008. InSAR processing for the recognition of landslides. Adv Geosci. 14: 189–194.

Rödelsperger S, Läufer G, Gerstenecker C, Becker M. 2010. Monitoring of displacements with ground-based microwave interferometry. IBIS-S and IBIS-L. 4(1):41–54.

Rosi A, Tofani V, Tanteri L, Tacconi Stefanelli C, Agostini A, Catani F, Casagli N. 2018. The new landslide inventory of Tuscany (Italy) updated with PS-InSAR: geomorphological features and landslide distribution. Landslides. 15(1):5–19.

Solari L, Barra A, Herrera G, Bianchini S, Monserrat O, Béjar-Pizarro M, Crosetto M, Sarro R, Moretti S. 2018. Fast detection of ground motions on vulnerable elements using Sentinel-1 InSAR data. Geomatics Nat Hazards Risk. 9(1):152–174.

Wang Y, Hong W, Zhang Y, Lin Y, Li Y, Bai Z, Zhang Q, Lv S, Liu H, Song Y. 2020. Ground-based differential interferometry SAR: A review. IEEE Geosci Remote Sens Mag. 8(1):43–70.

Wang Y, Jiang W, Li B, Luo Y, Li Y. 2021. Deformation monitoring and evaluation of mountain slope stability combined with ground-based radar and spaceborne InSAR methods.

Werner CL, Strozzi T, Wiesmann A, Wegmüller U, Kos A, Delaloye R, Raetzo H. 2010. Motion measurement of destabilized slopes in Switzerland with the GPRI-I ground-based real-aperture radar. AGU Fall Meeting Abstracts. G21A-0790.

Wu W, Hu J, Liu J, Li Z, Zhu J, Xu B, Zheng W, Zhang X. 2021. Derivation of high-quality three-dimensional surface deformation velocities through multi-source point cloud fusion: Application to Kīlauea volcano. Int J Appl Earth Obs Geoinf. 95:102270.

Xiao T, Huang W, Deng Y, Tian W, Sha Y. 2021. Long-term and emergency monitoring of zhongbao landslide using space-borne and ground-based InSAR. Remote Sensing. 13(8): 1578.

Zhang A, Lu J, Kim JW. 2018. Detecting mining-induced ground deformation and associated hazards using spaceborne InSAR techniques. Geomatics Nat Hazards Risk. 9(1):211–223.

Zhang Y, Meng X, Jordan C, Novellino A, Dijkstra T, Chen G. 2018. Investigating slow-moving landslides in the Zhouqu region of China using InSAR time series. Landslides. 15(7): 1299–1315.

Zhang Y, Meng XM, Dijkstra TA, Jordan CJ, Chen G, Zeng RQ, Novellino A. 2020. Forecasting the magnitude of potential landslides based on InSAR techniques. Remote Sens Environ. 241:111738.

Zhao C, Kang Y, Zhang Q, Lu Z, Li B. 2018. Landslide identification and monitoring along the Jinsha River catchment (Wudongde reservoir area), China, using the InSAR method. Remote Sensing. 10(7):993.

Zheng W, Hu J, Liu J, Sun Q, Li Z, Zhu J, Wu L. 2021. Mapping complete three-dimensional ice velocities by integrating multi-baseline and multi-aperture InSAR measurements: a case study of the Grove mountains area, East Antarctic. Remote Sensing. 13(4):643.